Journal of Applied Fluid Mechanics, Vol. 17, No. 10, pp. 2128-2140, 2024.
Available online at www.jafmonline.net, ISSN 1735-3572, EISSN 1735-3645.
https://doi.org/10.47176/jafm.17.10.2615

Study on the Performance of a Novel Air-bleeding Aerodynamic Combustor Diffuser

Y. Yan, D. Li, Y. Zhu, H. Liang†, J. Suo and Y. Wu

School of Power and Energy, Northwestern Polytechnical University, Xi`an 710072, China

†Corresponding Author Email: hx_liang@nwpu.edu.cn

ABSTRACT

The pressure ratio of a compressor increases when the engine performance is improved, which leads to a higher air velocity in the combustion chamber. This aggravates the pressure loss in a conventional diffuser, which is proportional to the square of the inlet velocity. It is, therefore, an urgent need for a new diffuser technology. Regardless of whether high-temperature, or low-pollution, combustion chambers are being used, the significant difference when compared with other chambers is the notable increase in the combustion air and its entry through the dome of the flame tube. However, the increased amount of air in the dome causes a mismatch between the diffuser outlet and the dome intake of the flame tube. Therefore, to solve the problem of an excessive total pressure loss and a mismatch of the intake air in the combustor, a novel air-bleeding aerodynamic diffuser has here been proposed. The effects of various parameters (including the number of air-bleed holes, the position of the first row of holes, and the position of the second row of holes) and their interactions on the performance of this diffuser have then been investigated by using the experimental design presented by Taguchi. The maximum static pressure recovery was achieved by using a genetic algorithm combined with the CFD method. Among the three parameters, the results revealed that the position of the first row of holes had the largest impact on the performance of the diffuser. Also, the optimal values of the three parameters varied for the inlet Mach numbers 0.10, 0.15, and 0.20. The relative difference between the predicted values and the values obtained by the numerical simulations were all below 3%, which showed the reliability of the predictions. As compared with the reference case, the optimized results for the three working conditions increased by 19.16%, 21.38%, and 40.62%, respectively.

Article History

Received January 25, 2024
Revised March 26, 2024
Accepted April 23, 2024
Available online July 31, 2024

Keywords:

Gas turbine combustor
Combustor diffuser
Diffuser performance
Optimization
Flow characteristics
Air bleeding aerodynamic diffuser

1. INTRODUCTION

With the development of the aviation industry, the pressure ratios of compressors have been gradually increased. As a result, the inlet air velocity into the combustor chambers has become increased. The pressure loss of the diffusers has also increased significantly since it is proportional to the square of the inlet velocity. Additionally, in both high-temperature and low-pollution combustion chambers, a considerable portion of the total combustion air (up to 80 percent or even more) needs to pass through the combustor dome (Chin, 2019), and all combustion air is required to enter from the head of the flame tube.

In the lean premixed pre-evaporation (LPP) combustion chamber, the airflow into the dome is regulated by increasing the head capture area to approximately 60% - 70%. The conventional faired diffuser shows low pressure losses, but this favourable characteristic is offset by several severe drawbacks that make this diffuser unsuitable for modern aircraft engines. For instance, the faired diffuser requires a considerable length and is very sensitive to variations in the inlet velocity profile (Klein, 1995). A dump diffuser has, therefore, been proposed to solve these problems, and it has been widely used. (Fishenden, 1977; Sanal Kumar *et al.*, 2007; Arvanid *et al.*, 2020). However, the dump diffuser is no longer appropriate when the dome intake increases. Shen *et al.* (2014) performed numerical simulations of the combustor diffusion system, and they

NOMENCLATURE

A	area of the total number of holes	R_r	radius of the holes
$c_{p\text{-}pre}$	predicted value of the static pressure recovery coefficient.	S_s	spreading spacing
$c_{p\text{-}ns}$	results of the numerical simulations of the static pressure recovery coefficient	T	inlet temperature
k	specific heat capacity	v_i	inlet velocity
L	length of the diffuser	W	width of the diffuser
L_f	start position of the first row of holes	W_d	distance between the center of the most marginal hole and the wall
L_s	start position of the second row of holes	X_1	dimensionless number of holes
m_d	airflow of the combustor head	X_2	dimensionless length for the start-position of the first row of holes
m_i	airflow of the inner annuli	X_3	dimensionless length for the start position of the second row of holes
m_o	airflow of the outer annuli	Y_1	static pressure recovery coefficient for working condition 1
n	number of holes	Y_2	static pressure recovery coefficient for working condition 2
p_{in}	static pressure at the diffuser inlet	Y_3	static pressure recovery coefficient for working condition 3
p_{out}	static pressure at the diffuser outlet	φ	entropy generation rate
R	gas constant	δ	relative difference between the predicted value and the numerically simulated value of the static pressure recovery coefficient

mainly focused on the effects of the cowling geometry, the area ratio of the pre-diffuser, and the axial length of the dump gap. It was then shown that both the spillage and total pressure loss decreased with a smaller cowl capture area. However, the spillage of air from the dome region into the inner and outer annuli was clear for an increased cowling capture area. This affected the flow besides the cowl, and resulted in a significant total pressure loss. He *et al.* (2013) presented experimental results where they showed that up to 60% of the airflow from the pre-diffuser flew into the dome. They found that the proportion of the pre-diffuser loss with respect to the overall loss was larger than for the conventional dump diffuser. Furthermore, Walker *et al.* (2009) studied the dump gap for a flow fraction of the compressor efflux, which entered into the combustor cowl, which was set to a representative lean module level (50% - 70%). Also, an optimization strategy for a novel dome geometric shape adjacent to the flame tube head has here been proposed, and the effective flow pattern and pressure distribution caused by the dome shape were analyzed using the ANSYS Fluent software (Rose *et al.*, 2023). The numerical data revealed that when the dump gap was required for the lean module injector, it was unlikely that the pre-diffuser would benefit from the flame tube blockage.

To reduce the total pressure loss in the diffuser, Liang *et al.* (2013), Zhao *et al.* (2014), and Li *et al.* (2012) designed a new distributor diffuser. Tests were conducted to investigate the influence of the distributor diffuser plate geometry. As a conclusion, the area ratio of the distributor diffuser was larger than for traditional diffusers, with a smaller construction and higher-pressure recovery performance. However, the flow loss through the distributor diffuser was not larger than the traditional limit. Moreover, Meng *et al.* (2020) and Guo *et al.* (2021) inserted short splitter vanes in the diffuser to improve the performance. The flow field in the diffuser, with and without a splitter vane, was also quantitatively analyzed. Even though this ensured that the airflow didn´t separate at large expansion angles, the friction loss increased accordingly. Therefore, the performance was not superior. Bohan *et al.* (2017) created successfully a variable geometry diffuser. They tested it for a number of diffuser feather positions and total inlet mass flow rates, with and without cavity combustion. When the variable geometry diffuser was tested for several equivalence ratios, and with different hybrid guide vanes, additional benefits of the variable diffuser were obtained. However, it is currently only used in ultra-compact combustion chambers. Guo *et al.* (2021) obtained length-to-area ratios of the flow separation zone in a diffuser with a fixed angle, with and without a splitter vane. Moreover, Adkins (1975) proposed a vortex-controlled diffuser and verified this diffuser with experimental data. Also, Smith *et al.* (1978) constructed a short annular dump diffuser by using suction-stabilized vortices. Adkins *et al.* (1980) reported on a hybrid diffuser, which was based on a hybrid arrangement of conventional and vortex-controlled diffusers. It was found to be efficient by Walker et al. (2004, 2005, 2009) and Srinivasan *et al.* (1990). The current problem is that the characteristics of the hybrid diffuser are not yet fully mastered, such as the design of the vortex chamber. There is also the problem that a part of the gas is being withdrawn, and there is a need to make up for this part of the cooling air. There is, therefore, an urgent need for a new type of diffuser to meet the demands of advanced combustion chambers.

When performing parametric studies, the design of experimental (DOE) method can be used for the design of important parameters. The effects of different parameters on the objectives can be, thereby, obtained. This will decrease the costs of the experiments. The objectives can

also be optimized by using the genetic algorithm method. This strategy has been widely used in the fields of chemistry and chemical engineering (Sun *et al.*, 2020), biology (Shen *et al.*, 2021), and food engineering (Wu *et al.*, 2022). In engineering, parameter optimizations have been conducted for use in blade film cooling (Zhang *et al.*, 2022). However, application in combustor diffusers has not yet been reported.

In the present study, a novel air-bleeding aerodynamic diffuser has been proposed and carefully designed by using the Taguchi approach (Taguchi, 1990). The effects of various parameters and their interactions on the performance of this diffuser have then been obtained. A genetic algorithm was used to obtain the values of three parameters for the achievement of the maximum static pressure recovery. The flow fields and entropy production, before and after optimization, were also analyzed and compared in detail.

For the novel air-bleeding aerodynamic combustor diffuser, this is the first time the DOE method has been used, and the first time the coupling between the different parameters of the diffuser has been obtained. Furthermore, this was the first time the optimal combination of parameters was obtained, thereby providing technical support for the design of air-bleeding aerodynamic combustor diffusers.

2. COMPUTATIONAL MODEL AND NUMERICAL SETUP

A numerical simulation method has been used in the present study. As presented in Fig. 1, the numerical simulation methodology consisted of building a model, generating a mesh, importing a fluent, selecting a solver, a solution method, boundary conditions, specified physical properties, an initialized flow field, and post-processing. It was also necessary to iterate and repeat this process.

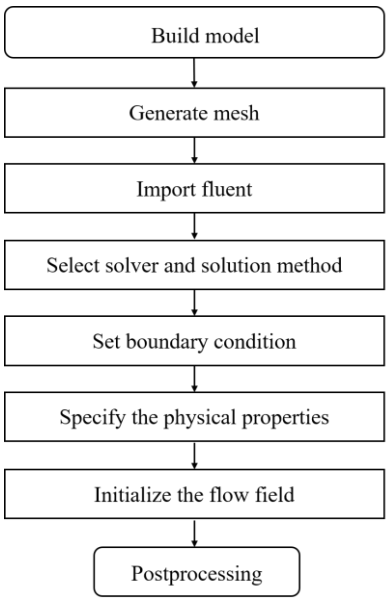

Fig. 1 Diagram of the numerical methodology

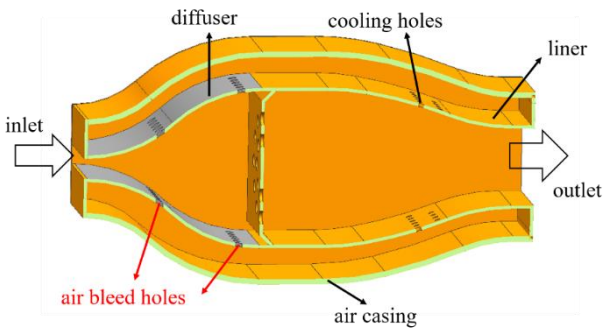

Fig. 2 Sketch of the air-bleeding aerodynamic diffuser

2.1 Parameter Design Method

Figure 2 presents a brief illustration of the air-bleeding aerodynamic diffuser, which is different from other types of diffusers (like conventional dump diffusers). This is because the air in this diffuser is bleeding through holes in the diffuser walls towards inner and outer channels, and is being used as a liner cooling air. Most of the air passes through the dome as combustion air. Also, the profile of the diffuser is a tangent double arc, where the opening direction of the holes is perpendicular to the incoming flow direction.

In the present study, the effect of the openings in the diffuser walls has been studied by changing the number of holes, the start position of the first row of holes, and the start position of the second row of holes. The following constraints were then used;

$$R_r = \sqrt{\frac{A}{\pi \times n}} \tag{1}$$

$$R_r < L_f < \frac{L}{2} - R_r \tag{2}$$

$$R_r < L_s < \frac{L}{2} - R_r \tag{3}$$

$$2R_r < S_s < \frac{W - W_d \times 2 - R_r \times 2}{\frac{n}{2} - 1} \tag{4}$$

where R_r is the radius of the holes, A is the total area of the holes (765 mm^2), n is the number of holes, and S_s is the spreading spacing. In addition, L, L_f, and L_s are the length of the diffuser (157 mm), the start position of the first row of holes, and the start position of the second row of holes, respectively. Also, W is the width of the diffuser (170 mm) and W_d is the distance between the center of the most marginal hole and the wall.

A three-level Taguchi experimental design was used to obtain the flexural properties of the factors n, L_f, and L_s. Based on the constraints presented in eqs. 1-4 and the geometric limitations, the upper and lower limits of the number of holes, start position of the first row of holes, and start position of the second row of holes were then calculated. As a result, the high and low levels of these three factors were 4 - 40, 23 mm – 70 mm, and 16 mm –

Table 1 Experimental design for a series of cases

Item	Number of holes	Start position of the holes (mm)	Second position of the holes (mm)
Case-1 (reference)	4	23	16
Case-2	4	46.5	35.5
Case-3	4	70	55
Case-4	22	23	35.5
Case-5	22	46.5	55
Case-6	22	70	16
Case-7	40	23	55
Case-8	40	46.4	16
Case-9	40	70	35.5

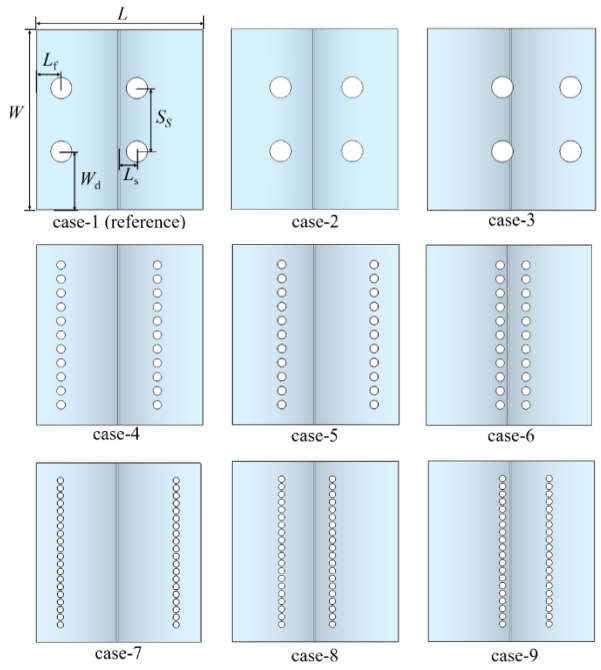

Fig. 3 Illustrations of the diffuser for different cases

55 mm, respectively. The experimental design is presented in Table 1 for a series of cases. Also, illustrations of the diffuser for different cases are presented in Fig. 3.

2.2 Governing Equations

In the present study, the RANS method (Jiang, 2017) has been used to numerically simulate the performance and flow field of an air-bleeding aerodynamic diffuser. The ANSYS Fluent software was used for these simulations, together with various structural parameters. By using Cartesian coordinates, the governing equations that were required for these simulations are presented below.

Mass conservation equation:

$$div(\rho\vec{v}) = 0 \tag{5}$$

Momentum conservation equation:

$$\frac{\partial(\rho u)}{\partial t} + div(\rho u\vec{v}) = div(\mu gradu) - \frac{\partial P}{\partial x} + S_u \tag{6}$$

$$\frac{\partial(\rho v)}{\partial t} + div(\rho v\vec{v}) = div(\mu gradv) - \frac{\partial P}{\partial y} + S_v \tag{7}$$

$$\frac{\partial(\rho w)}{\partial t} + div(\rho w\vec{v}) = div(\mu gradw) - \frac{\partial P}{\partial z} + S_w \tag{8}$$

Energy conservation equation:

$$\frac{\partial(\rho T)}{\partial t} + div(\rho\vec{v}T) = div(\frac{k}{c_p} gradT) + \frac{S_T}{c_p} \tag{9}$$

State equation:

$$\rho = f(p, T) \tag{10}$$

Finally, the time average of the momentum equation was used to obtain the Reynolds equation (expressed with tensor subscripts):

$$\rho\frac{\partial u_i}{\partial t} + div(\rho v\vec{v}) = \frac{\partial}{\partial x_j}(\mu\frac{\partial u_i}{\partial x_j} - \rho\overline{u_i' u_j'}) - \frac{\partial P}{\partial x_i} + S_i \tag{11}$$

The system of equations that described the turbulent motion was not closed, which was due to the use of time averaging. Also, it was necessary to use a turbulence model for new unknown quantities that appeared in the system of equations, thereby adding additional equations to make the system of equations closed. Among the turbulence models that are provided by the ANSYS Fluent software, the Reynolds-averaged N-S system of equations (RANS) is the most widely used one for mature engineering turbulence problems. RANS is based on the eddy-viscous closed-mode theory, mainly including zero-equation, one-equation, and two-equation models (such as k-ε, k-ω, etc.). In the present study, the two-equation model has been used to close the equations.

2.3 Boundary Conditions

The boundary conditions for the various cases are presented in Table 2. The diffuser inlet had a temperature of 300 K and mass flow rates of 0.1179 kg/s, 0.1976 kg/s, and 0.2620 kg/s. By considering the density of the dry air and the initial velocity of the inlet air, the Mach number was calculated as:

$$Ma = v_i / \sqrt{kRT} \tag{12}$$

where v_i represents the inlet velocity, and R and k represent the gas constant and specific heat capacity, respectively. Also, T is the inlet temperature (300 K).

2.4 Mesh

As can be seen in Fig. 4, a tetrahedral unstructured mesh was used for all cases by using ICEM CFD 2020 R1

Table 2 Boundary conditions for the cases

Zone	Type	Value
Inlet	Mass flow-inlet	0.1179, 0.1976, and 0.2620 (kg/s)
Outlet	Pressure-outlet	-1575 (Pa)
Walls	No-slip	---

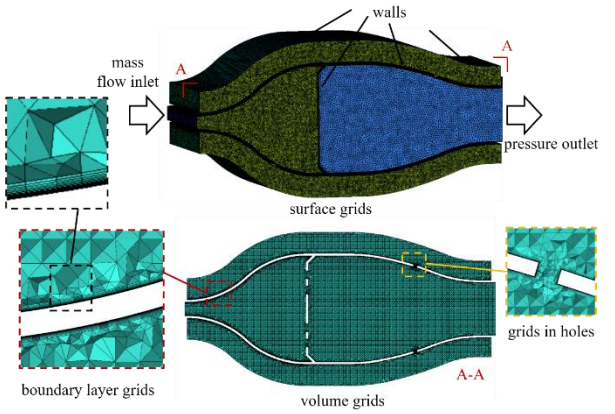

Fig. 4 Grid systems in the computational domain of the diffuser

(Ji *et al.*, 2015), with a quality higher than 0.2. The first height of the boundary layer was 0.01. To ensure that the y+ value was smaller than 5, the growth ratio was set to 1.2 and the number of boundary layer mesh layers was set to 15.

Moreover, three grid cell counts that ranged from 6.0 million to 19.0 million were created (coarse grid = 6.0×10^6, medium grid = 10.9×10^6, and fine grid = 19.0×10^6). For the medium grid and fine grid, the axial velocity distributions 10 mm in front of the head flange were found to match (Fig. 5). The medium grid size (10.9×10^6 cells) was, therefore, selected for the numerical study.

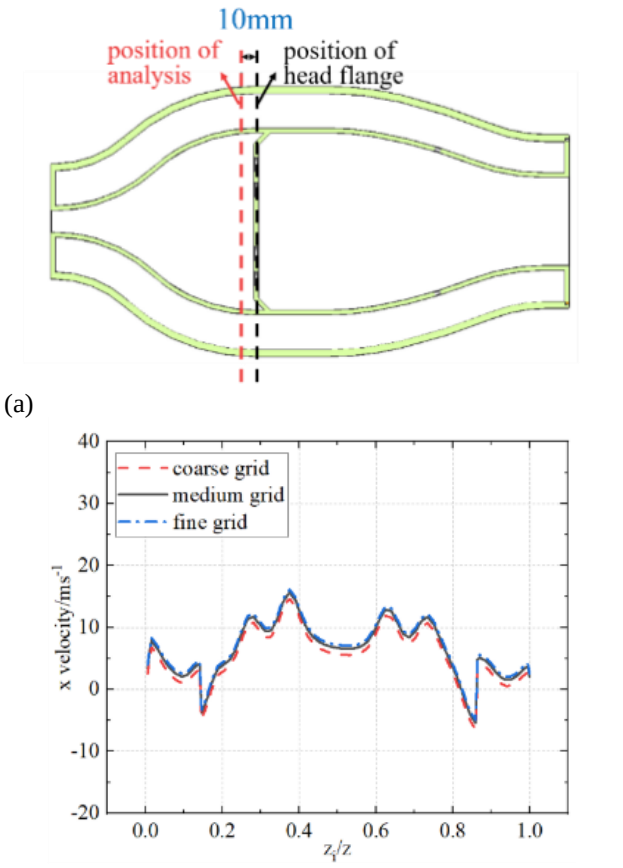

Fig. 5 Grid independence test; (a) Axial position and (b) axial velocity distribution

2.5 Validation

In the present study, the experimental results that were obtained in the study by Chen (1989) have here been chosen for the validation of the numerical method. The experiment in this earlier study was carried out in an aspirated two-dimensional diffuser wind tunnel. This tunnel consisted of a lemniscate inlet, upper and lower diffuser walls, adjustable screws, left and right Plexiglas sidewalls, a transfer section, and valves connected to the vacuum pump piping. Wall static pressure measurements were then performed, with a 0.8 mm diameter copper tube along the centerline of the diffuser wall and perpendicular to the buried wall. There were also 22 hydrostatic holes from the inlet to the outlet of the diffuser. The pressure was measured by an internal 48-point pressure scanning valve, which was equipped with a filament pressure sensor. It was during this experiment found that the diffuser was too large, which was due to the initial expansion angle. The airflow in a serious separation as soon as it enters the diffuser, the performance will be very poor, so the initial expansion is called to reduce. It was also found that the theoretically calculated distribution of the static pressure recovery differed to a large extent from the results of the experimental test. The reason was that the theoretically calculated momentum integral equation of the attached surface layer did not consider the effect of wall curvature. The wall curvature was considered in the calculations finally. The boundary conditions in the present study align with those of the experiments in the Chen *et al.* (1989). Furthermore, the physical model was the same as in the experiments, and the three turbulence models shear stress transport k-ω (SST-kω), standard k-ε (skε), and realistic k-ε (rkε) were validated and compared. As can be seen in Fig. 6, the calculated results by using the SST-kω turbulence model, and the enhanced wall function yield, showed that the simulations were accurate for the entire diffuser. The maximum error was not larger than 10.62%. The model was treated differently near the wall and away from the wall, which made the calculations more credible. Therefore, the following model was used in the present study for the numerical calculations: An SST-kω turbulence model with a mass flow inlet, pressure outlet, SIMPLE solver (Yan *et al.*, 2011), second-order windward scheme, and non-structural mesh parameters.

2.6 Objective Parameters

In the present optimization, the objective function has been used to maximize the coefficient of the mass-averaged static pressure recovery. This coefficient was then calculated by averaging the values over the downstream region of the diffuser and the annular

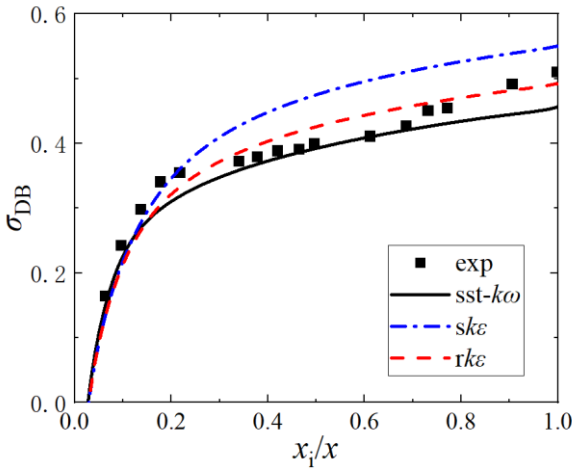

Fig. 6 Comparison of results from the numerical simulations and the experiment

channels:

$$c_{PR}=\frac{m_d p_d+m_o p_o+m_i p_i-(m_d+m_o+m_i)p_{in}}{\frac{(m_d+m_o+m_i)}{2}\rho v_i^2} \tag{13}$$

where p_{in} is the static pressure at the diffuser inlet, p_{out} is the static pressure at the diffuser outlet, and m_d is the airflow of the combustor head. In addition, m_o is the airflow of the outer annuli and m_i is the airflow of the inner annuli.

Furthermore, the entropy generation rate (φ) was used to obtain the amount of loss in the flow field. It primarily described the magnitude of the generation of loss, which resulted from the heat transfer and viscous shear stress of the fluid. In the isothermal flow, the heat transfer was neglected and the viscous shear stress component was divided into mean flow and fluctuations. The distribution of the entropy generation rate provided an insight into the relationship between the flow structure and loss generation, and, thus, the mechanism of the irreversible flow loss. This could be defined by the following equation:

$$\varphi=\frac{\mu}{T}\left\{\begin{array}{l}2\left[\left(\frac{\partial u}{\partial x}\right)^2+\left(\frac{\partial v}{\partial y}\right)^2+\left(\frac{\partial w}{\partial z}\right)^2\right]+\\ \left(\frac{\partial u}{\partial y}+\frac{\partial v}{\partial \omega}\right)^2+\left(\frac{\partial v}{\partial z}+\frac{\partial w}{\partial y}\right)^2+\left(\frac{\partial u}{\partial z}+\frac{\partial w}{\partial x}\right)^2\end{array}\right\} \tag{14}$$

where the right side of the equation represents the line deformation and angular deformation of the fluid microclusters in three directions (i.e., *x*, *y*, and *z*).

3. OPTIMIZATION PROCEDURE

The optimization procedure is presented in Fig. 7. At first, the design space was accurately determined by establishing constraints in the definition of the lower and upper limits of the design variables. As the next step, 9 sampling cases were generated by using an orthogonal experimental 3-level design with 3 parameters (Table 1). Also, the mass-averaged static pressure recovery was obtained by performing CFD simulations. Regression

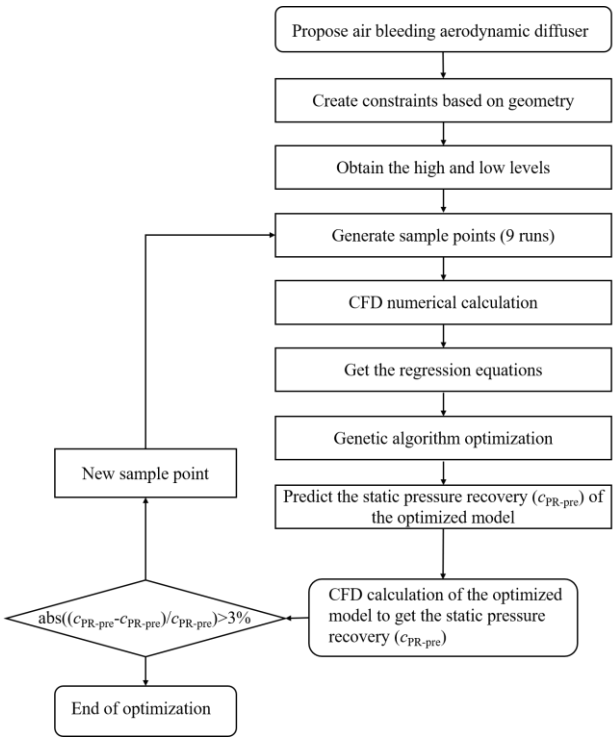

Fig. 7 Optimization scheme

equations, which correlated the objective results with the design variables, were also constructed. The multi-island genetic algorithm was used to optimize the parameters and to predict the maximum mass-averaged static pressure recovery $c_{PR\text{-}pre}$. The optimal $c_{PR\text{-}pre}$ values were compared with the $c_{PR\text{-}CFD}$ value to ensure the accuracy of the results. The $c_{PR\text{-}CFD}$ value was obtained by performing a new CFD simulation using the optimized parameters. When the relative error between $c_{PR\text{-}pre}$ and $c_{PR\text{-}CFD}$ was smaller than 0.03, the results were regarded as acceptable and the optimization procedure ended. If this was not the case, the experimental design, regression equation construction, optimization prediction, and CFD validation were repeated until the convergence criterion was met. Finally, the optimized result was compared with the result of the reference model.

The genetic algorithm, which is a global optimization algorithm, has here been used to obtain the optimal parameters. As first proposed by Holland (1975), this is an optimization algorithm for the biological evolutionary process. It is generally used for simulating the natural selection and genetic mechanism of Darwin's biological evolution theory. By using this genetic algorithm, and after that the initial population has been generated, a generation by generation is being evolved in the creation of an increasingly improved solution according to the survival of the fittest principle. For each generation, the individuals are then selected according to their fitness in the problem domain. A combinatorial crossover and mutation were then obtained with the help of natural genetic operators in the creation of a population that represented a new set of solutions. Like natural evolution, this process resulted in a population that was more adapted to the environment than previous generations. The optimal individual in the last generation of population was

Table 3 Coefficients of the static pressure recovery for nine models

Item	Static pressure recovery coefficients		
	Inlet Mach number=0.10	Inlet Mach number=0.15	Inlet Mach number=0.20
Case-1 (reference)	0.5547	0.5594	0.5248
Case-2	0.6552	0.6349	0.6709
Case-3	0.6294	0.6598	0.6660
Case-4	0.5674	0.5707	0.5860
Case-5	0.6041	0.6463	0.6120
Case-6	0.5496	0.4934	0.6820
Case-7	0.5883	0.5773	0.5983
Case-8	0.6059	0.6454	0.6570
Case-9	0.5258	0.5104	0.5596

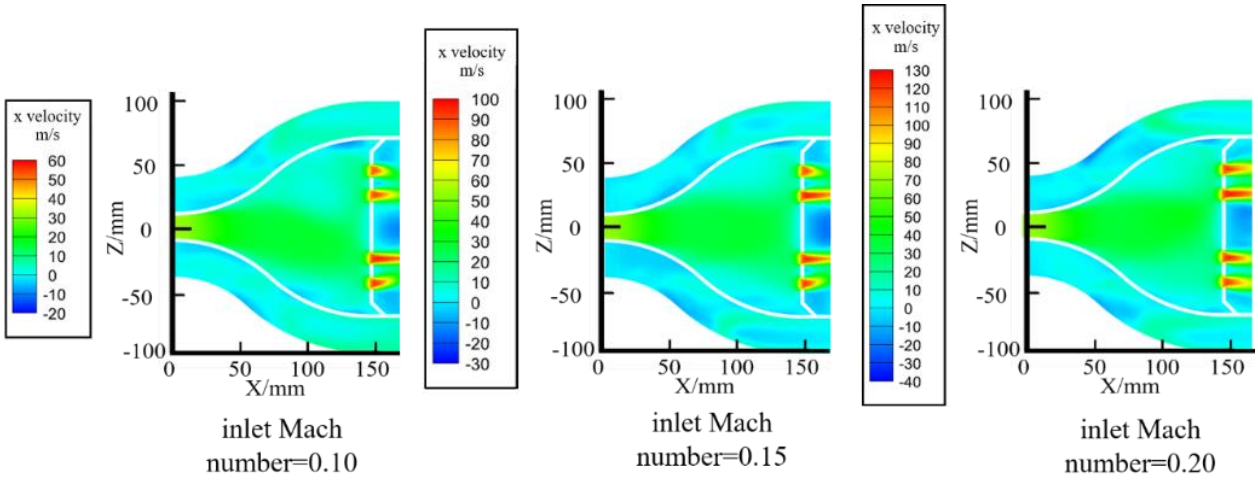

Fig. 8 Axial velocity contours of the reference model under three working conditions

decoded and could be used as an approximate optimal solution to the problem. According to the survival of the fittest principle, after the initial generation of a population, the evolution of generation by generation resulted in an improved approximation of the solution. For each generation, the individuals were selected according to their fitness in the problem domain. The population that represented a new set of solutions was generated by crossover and mutation with the help of genetic operators of natural genetics.

According to the fitness of the individuals in the problem domain of individuals, and with the help of natural genetic operators to carry out crossover and mutation, each generation represented a set of solutions. This process resulted in a naturally evolving population, where later generations were more adapted to the environment than previous ones. The best individuals in the last generation of the population were decoded and could be used as a near-optimal solution to the problem.

4. RESULTS AND DISCUSSION

4.1 Performance of Different Cases

The coefficients of the static pressure recovery for nine models under three different working conditions are presented in Table 3. These coefficients typically ranged from 0.5 to 0.7. Also, the performance parameters of the diffuser varied with the changes in the structural and pneumatic parameters. It was also observed that when using Taguchi's experimental design method, the impact of different factors on the response was not clearly apparent.

4.2 Analysis of the Reference Case

The reference model has here been used for the analysis of the flow field inside the air bleeding aerodynamical diffuser. As can be seen in Fig. 8, the axial velocity contours of the reference model under three different working conditions had a basically symmetric flow field structure. The flow field structure inside the air-bleeding aerodynamic diffuser remained constant for different working conditions, with the airflow entering the diffuser inlet and most of it flowing into the flame tube through the dome intake holes (Chin, 2019). A small portion of the airflow entered the inner and outer annuli through the holes. It, thereafter, entered the flame tube through the cooling holes to take part in the cooling and mixing process.

Figure 9 presents the distribution of the axial velocity for a radial position 10 mm in front of the head flange. The horizontal axis represents the dimensionless radial position, while the vertical axis represents the axial velocity. The velocity distribution under different working conditions showed basically the same trend. The axial velocity of the airflow reached a local minimum near z_i/z

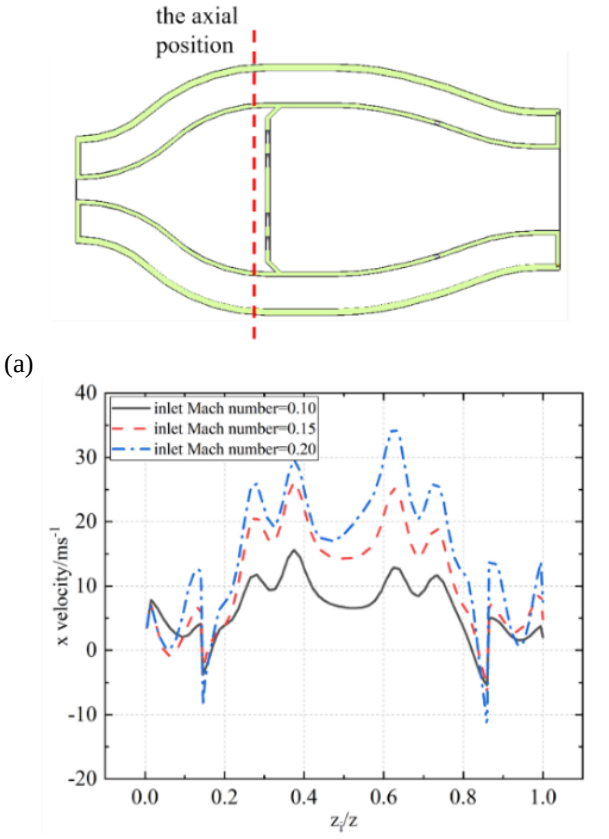

Fig. 9 Distribution of the axial velocity with a radial position 10 mm in front of the head flange; (a) Axial position and (b) axial velocity distribution

= 0.5, which corresponded to the radial center position. There were two peaks on the outer radial side, where the airflow from the head inlet hole flew, which resulted in a higher velocity. Furthermore, there was a negative axial velocity towards the outer radial side. This was an indication of an airflow into the inner and outer annuli, where it formed a vortex.

These were the contours of the entropy production rate of the reference model under different working conditions (Fig. 10). As the inlet velocity increased, the area of the high entropy yield in the diffuser expanded, which led to a larger peak of the entropy yield. The high entropy yield in the diffuser was primarily distributed in the areas that are marked with A, B, and C in Fig. 10. Area A was near the wall in the diffuser, and the high entropy yield in this area was due to friction loss. Also, area B showed the loss generated by the deflection of the airflow from the holes of the diffuser surface. Finally, area C showed the loss generated by the throttling of the airflow as it flew into the intake holes of the head.

4.3 Fitting of the Results

According to the numerical simulation results presented above, the quadratic regression model of the coefficient of the static pressure recovery in the diffuser was obtained for different inlet velocities:

Working condition 1:

$$Y_1 = 0.3330 + 0.000398X_1 + 0.010775X_2 + 0.002416X_3 + 0.000060X_1^2 - 0.000095X_2^2 - 0.000034X_3^2 - 0.000089X_1X_2 \quad (15)$$

Working condition 2:

$$Y_2 = 0.39485 + 0.006291X_1 + 0.011614X_2 - 0.005205X_3 - 0.000146X_2^2 - 0.000004X_3^2 - 0.000126X_1X_2 + 0.000123X_2X_3 \quad (16)$$

Working condition 3:

$$Y_3 = 0.2419 + 0.00813X_1 + 0.01285X_2 + 0.00205X_3 - 0.000079X_2^2 - 0.000055X_3^2 - 0.000184X_1X_2 \quad (17)$$

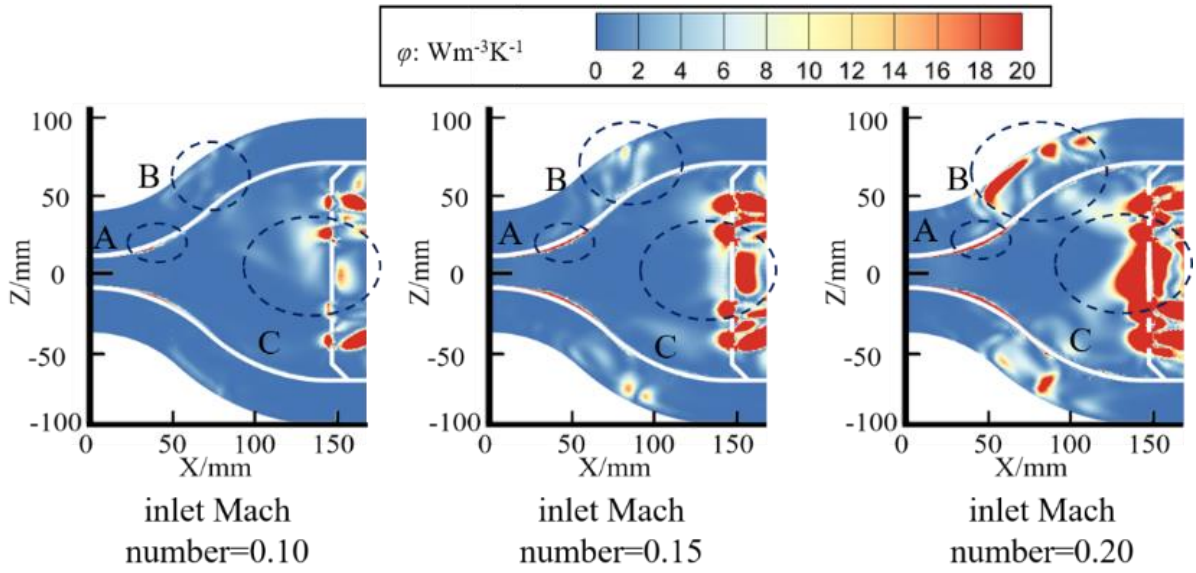

Fig. 10 Entropy production rate contours of the reference model under three working conditions

where X_1 is n divided by the dimensionless value of the unit of quantity. X_2 is L_f divided by the dimensionless value of the unit of length. Also, X_3 is L_s divided by the dimensionless value of the unit of length. Furthermore, Y_1, Y_2, and Y_3 are the coefficients of the static pressure recovery under different working conditions.

Tables 4-6 present the ANOVA results (Xiang *et al.*, 2014) when using the regression model for the three working conditions with the Mach numbers 0.10, 0.15, and 0.20, respectively. In these tables, A denotes the number of air bleed holes, B denotes the position of the first row of air bleed holes, and C denotes the position of the second row of air bleed holes. The R-sq values for the Mach numbers 0.10, 0.15, and 0.20 were 99.12%, 99.99%, and 98.39%, respectively. The regression model was highly significant, with no signs of model misfit. Also, the statistical variable P in Tables 4-6 showed the effect of each variable on the final response. A value smaller than 0.05 indicated that the variable had a significant effect on the response, and a value larger than 0.10 indicated that the variable had basically no effect on the response (Wu *et al.*, 2022). Furthermore, it could be seen that the parameters that had the largest impact on the performance of the diffuser were different for the three operating conditions.

Figures 11-13 show Pareto charts that illustrate the standardization effect under different operating conditions. These charts were primarily used to determine which of the intrinsic components of the variable was most important. There was then a focus on the most important component for the improvement of the quality of the process. The Pareto charts, also known as ranked charts and principal and secondary factor charts, are bar charts that are arranged in descending order. As being arranged as a cumulative percentage curve, the lengths of the bars indicate the size of the absolute number in each group. Also, the bars are arranged in descending order to

Table 4 Analysis of the variance for the inlet Mach number 0.10

Source	Degree of freedom	Adj. SS	Adj. MS	F value	P value
Regression	7	0.013658	0.001951	129.52	0.068
A	1	0.000010	0.000010	0.67	0.564
B	1	0.007332	0.007332	486.72	0.029
C	1	0.000290	0.000290	19.22	0.143
A*A	1	0.000761	0.000761	50.52	0.089
B*B	1	0.005524	0.005524	366.69	0.033
C*C	1	0.000271	0.000271	18.01	0.147
A*B	1	0.002853	0.002853	189.41	0.046
Error	1	0.000015	0.000015	/	/
Total	8	0.013673	/	/	/

Table 5 Analysis of the variance for the inlet Mach number 0.15

Source	Degree of freedom	Adj. SS	Adj. MS	F value	P value
Regression	7	0.030262	0.004323	7793.20	0.009
A	1	0.003966	0.003966	7148.95	0.008
B	1	0.007861	0.007861	14170.50	0.005
C	1	0.001207	0.001207	2175.78	0.014
B*B	1	0.012922	0.012922	23294.16	0.004
C*C	1	0.000004	0.000004	7.41	0.224
A*B	1	0.004519	0.004519	8146.00	0.007
B*C	1	0.006382	0.006382	11504.94	0.006
Error	1	0.000001	0.000001	/	/
Total	8	0.030262	/	/	/

Table 6 Analysis of the variance for the inlet Mach number 0.20

Source	Degree of freedom	Adj. SS	Adj. MS	F value	P value
Regression	6	0.023589	0.003931	11.48	0.082
A	1	0.010077	0.010077	29.42	0.032
B	1	0.010421	0.010421	30.42	0.031
C	1	0.000208	0.000208	0.61	0.518
B*B	1	0.003846	0.003846	11.23	0.079
C*C	1	0.000711	0.000711	2.08	0.286
A*B	1	0.012134	0.012134	35.42	0.027
Error	2	0.000685	0.000343	/	/
Total	8	0.024274	/	/	/

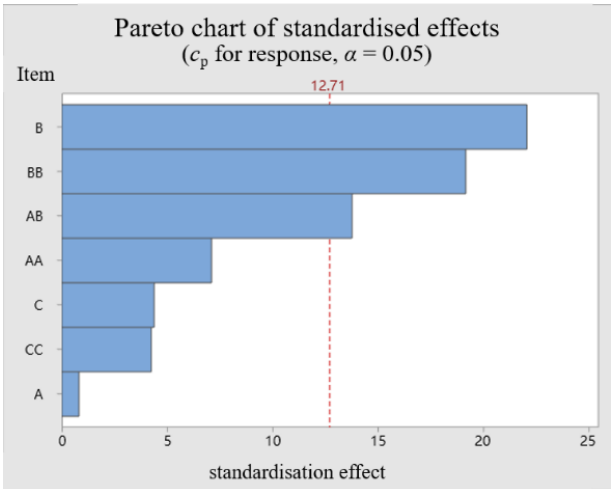

Fig. 11 Pareto chart of standardized effects for the inlet with the Mach number 0.10

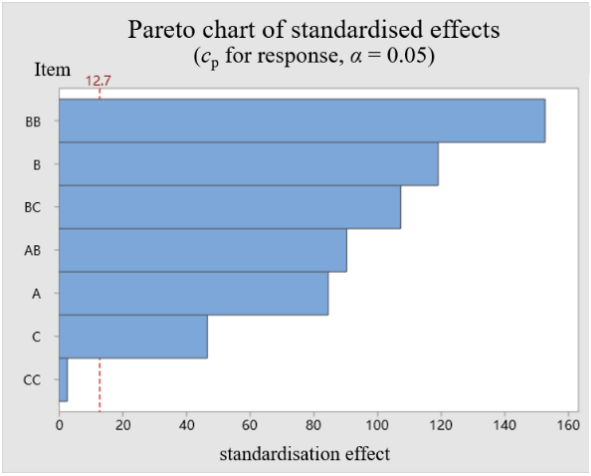

Fig. 12 Pareto chart of standardized effects for the inlet with the Mach number 0.15

visualize the major and minor factors. As can be seen in Figs. 11-13, when the inlet flow rate was low, there were three factors that had a significant impact on the performance of the air-bleeding aerodynamic diffuser. The effects were arranged from the largest to the smallest, and were obtained for items B, BB, and AB. For the second condition, there were six factors that had a significant impact on the performance of the air-bleeding aerodynamic diffuser. These effects were represented by BB, B, BC, AB, A, and C in descending order. There were also three factors that significantly affected the performance of the air-bleeding aerodynamic diffuser under a maximum operating condition. These effects were represented by AB, B, and A in descending order. As can be seen in Figs. 11-13, it was clear that the first row of air-bleed holes played a crucial role under the different operating conditions. This was probably due to its role in the determination of the flow state of the main airflow. There was also an interaction factor that affected the performance of the air-bleeding aerodynamic diffuser. This was an indication of a secondary role of the structural parameters in affecting the performance of the diffuser. In addition, there was a coupling between the different structural parameters (in particular for AB). That is, the

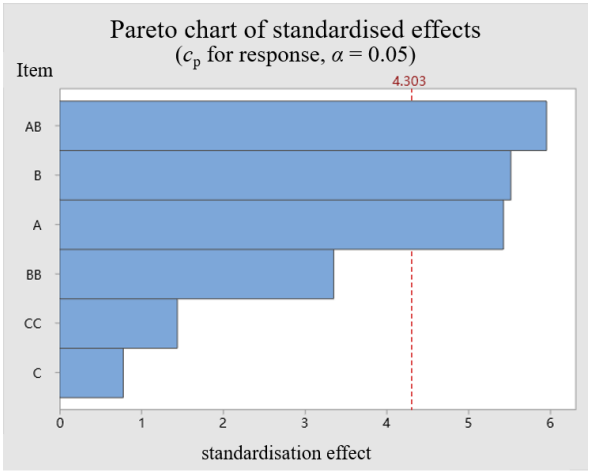

Fig. 13 Pareto chart of standardized effects for the inlet with the Mach number 0.20

coupling between the number of holes and the position of the first row of air-bleed holes had a notable effect on the coefficient of the static pressure recovery of the diffuser.

4.4 Optimization Results

To obtain geometrical parameters for the optimal performance of the air-bleeding aerodynamic diffuser at various inlet velocities, the results for the three conditions have been optimized and analyzed by using a genetic algorithm. The iterative results that were obtained by using the maximum static pressure recovery coefficient at different conditions are presented in Table 7. Also, Figs. 14-16 show the model, axial velocity distribution contours, and entropy yield distribution contours for the optimal parameters under the three working conditions. The relative differences were calculated by using the following equation:

$$\delta = \frac{|c_{\text{p-pre}} - c_{\text{p-ns}}|}{c_{\text{p-ns}}} \times 100\% \tag{18}$$

where $c_{\text{p-pre}}$ is the predicted value of the static pressure recovery coefficient and $c_{\text{p-ns}}$ is the numerically calculated static pressure recovery coefficient.

As compared with the baseline model, the optimization results showed a 19.16% larger static pressure recovery coefficient for an inlet Mach number of 0.10. Also, the relative difference was 0.45%. When the inlet Mach number was 0.15, the static pressure recovery coefficient became 21.38% higher than that of the baseline model, with a relative difference of 1.03%. Furthermore, when the inlet Mach number was 0.20, the static pressure recovery coefficient was 40.62% higher than that of the baseline model, with a relative difference of 2.17%.

5. CONCLUSION

The design method by Taguchi has here been combined with an experimentally verified numerical simulation method in an investigation of the effects of various structural parameters and their interactions on the performance of a novel air-bleeding aerodynamic diffuser. These parameters included the number of air-bleed holes,

Table 7 Optimization results for different inlet Mach numbers

Inlet Mach number	Numbers of the holes	Start position of the holes	Second position of the holes	$c_{p\text{-}pre}$	$c_{p\text{-}ns}$	δ (%)
0.10	4	54.84	35.53	0.664	0.661	0.45
0.15	40	29.25	16	0.686	0.679	1.03
0.20	4	70	18.64	0.754	0.738	2.17

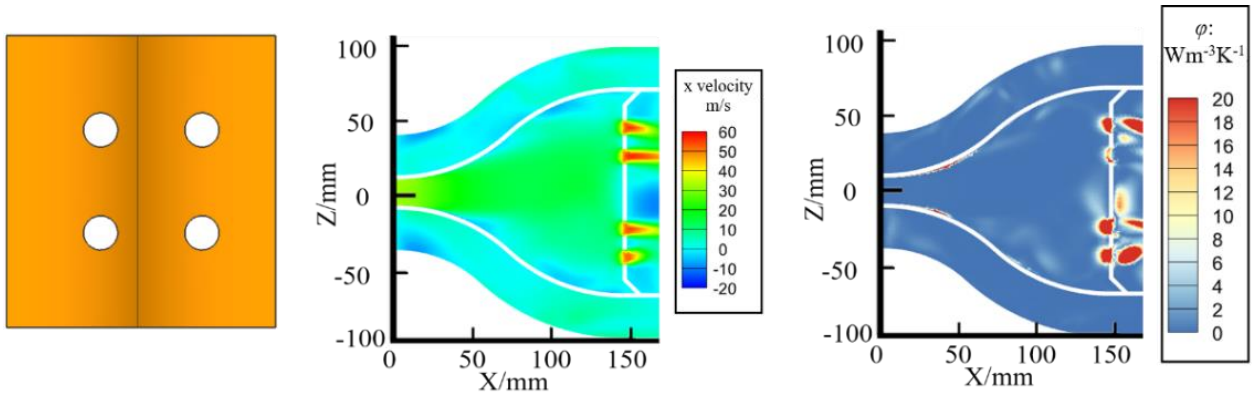

(a) (b) (c)

Fig. 14 Optimization results for an inlet Mach number of 0.10; (a) Model of the optimal diffuser, (b) axial velocity distribution contours, and (c) entropy yield distribution contours

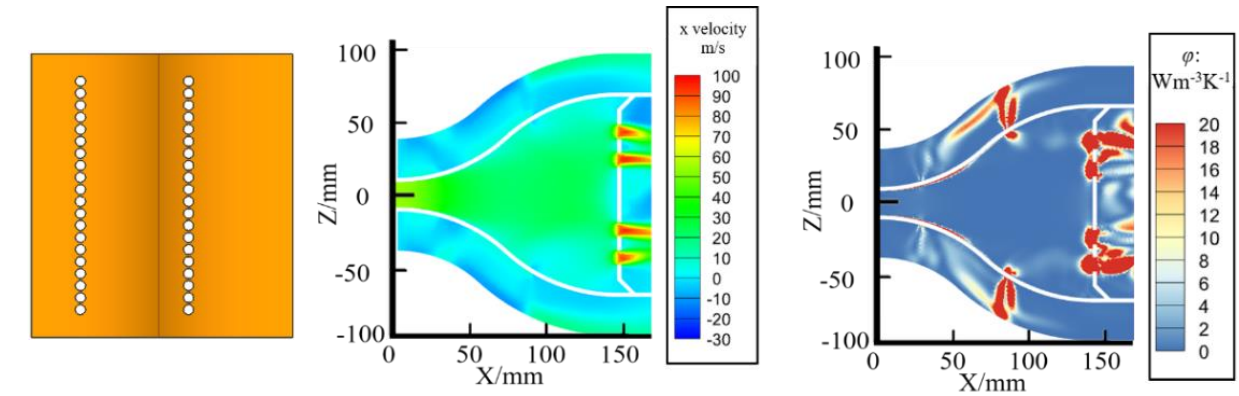

(a) (b) (c)

Fig. 15 Optimization results for an inlet Mach number of 0.15; (a) Model of the optimal diffuser, (b) axial velocity distribution contours, and (c) entropy yield distribution contours

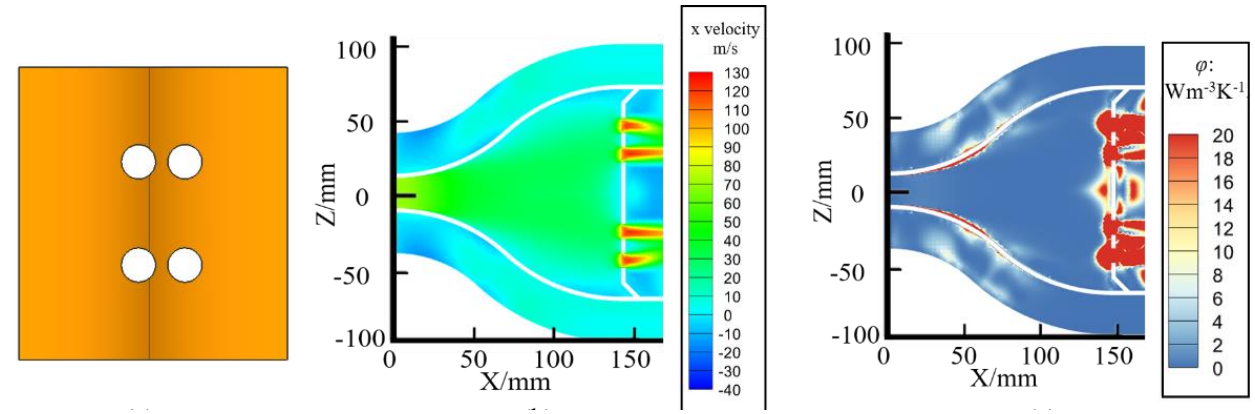

(a) (b) (c)

Fig. 16 Optimization results for an inlet Mach number of 0.20; (a) Model of the optimal diffuser, (b) axial velocity distribution contours, and (c) entropy yield distribution contours

the position of the first row of holes, and the position of the second row of holes. Regression equations for the coefficient of the static pressure recovery and the structural parameters were then obtained. By using a genetic algorithm, an optimization of the different holes was conducted to obtain the optimized structural parameters. From the results of the present study, the following specific conclusions could be drawn:

(1) Among the three structural parameters (number of air bleed holes, position of the first row of holes, and position of the second row of holes) it was the position of the first row of holes that had the largest impact on the performance of the diffuser.

(2) For the inlet Mach numbers 0.10, 0.15, and 0.20, the optimal values of the three parameters were different (0.661, 0.679, and 0.738, respectively).

(3) The relative difference between the predicted values and the numerical simulation results were 0.45%, 1.02%, and 2.12%, respectively, which were all smaller than 3%. Thus, the predicted results were reliable.

In the future, the air bleeding aerodynamic diffuser will be studied when used in a real combustion chamber, which will lay the foundation for subsequent application in real engines.

ACKNOWLEDGEMENTS

The authors disclosed receipt of the following financial support for the research, authorship, and/or publication of this article: The authors would like to thank the support by the National Science and Technology Major Project (Grant No.J2019-III-0022-0066) the National Science and Technology Major Project (J2019-Ⅲ-0012-0055).

The authors would like to express their gratitude to EditSprings (https://www.editsprings.cn) for the expert linguistic services provided.

CONFLICT OF INTEREST

The authors declare that they have no conflicts of interest.

AUTHORS CONTRIBUTION

Yue Yan performed methodology and writing. **Donghui Li** performed data curation and validation. **Youwen Zhu** performed formal analysis and resources. **Jianqin Suo**, **Hongxia Liang**, and **Yanhui Wu** performed review and edit.

REFERENCES

Adkins, R. C. (1975). A short diffuser with low pressure loss. *Journal of Fluids Engineering, 97*(3), 297-302. https://doi.org/10.1115/1.3447306.

Adkins, R. C., Matharu, D. S., & Yost, J. O. (1980, March 10-13). *The hybrid diffuser*. Proceedings of the ASME 1980 International Gas Turbine Conference and Products Show. https://doi.org/10.1115/80-gt-136.

Arvanid, S., Sabarinathan, G., Dhinakaran, S., & Sanjay Kumar, S., Sundararaj, K. & Sanal Kumar, V. R. (2020, August 24-28). *Design optimization of dump diffusers with NACA 66-021 shaped flame tube*. AIAA Propulsion and Energy Forum. https://doi.org/10.2514/6.2020-3705.

Bohan, B. T., & Polanka, M. D. (2017, Januray 9-13). *Development and testing of a variable geometry diffuser in an ultra-compact combustor*. 55th AIAA Aerospace Sciences Meeting, AIAA 2017-0777. https://doi.org/10.2514/6.2017-0777.

Bruce Ralphin Rose, J., & Prawin, L. (2023). Numerical characterization on the influence of flame tube geometry and dump gap in the diffuser performance at high altitudes. *Proceeding of the National Academy of Sciences, India Section A: Physical Sciences*, *94*(1), 47-61. https://doi.org/10.1007/s40010-023-00865-5

Chen, X. (1989). Experimental investigation on improvement of performance of subsonic two dimensional diffuser. *Journal of Propulsion and technology*, *1989*(03), 30-35. https://doi.org/CNKI:SUN:TJJS.0.1989-03-005.

Chin, J. (2019, August 19-22). *Suggestions on high temperature rise combustor*. Proceedings of the AIAA Propulsion and Energy 2019 Forum. https://doi.org/10.2514/6.2019-4327.

Fishenden, C. R. (1977). Performance of annular combustor-dump diffuser. *Journal of Aircraft*, *14*(1), 60-67. https://doi.org/10.2514/3.58749.

Guo, M., Meng, X., Zuo, Z. G., & Liu, S. H. (2021). Experimental influence of a splitter vane on the flow fields in a wide-angled diffuser. *2021 IOP Conference Series: Earth Environmental Science*, 774 012051. https://doi.org/10.1088/1755-1315/774/1/012051.

He, P., Suo, J. Q., Xie, K., Chen, S., Shen, S., & Zeng, Q. (2013, June 3-7). *The influence of dump gap on aerodynamic performance of a low-emission combustor dump diffuser*. Proceedings of ASME Turbo Expo 2013: Turbine Technical Conference and Exposition, 18. https://doi.org/10.1115/gt2013-95230.

Ji, B. B., Zhang, X. X., & Gu, Y. (2015). *ANSYS ICEM CFD basic tutorials and examples*. Machinery Industry Press.

Jiang, L. Y. (2017). *RANS modelling of turbulence in combustors*. Turbulence Modelling Approaches - Current State, Development Prospects, Applications. https://doi.org/10.5772/intechopen.68361.

Klein, A. (1995). Characteristics of combustor diffusers. *Progress in Aerospace Sciences*, *31*, 171-271. https://doi.org/10.1016/0376-0421(95)00006-K.

Li, H., Suo, J. Q., Liang, H. X., Li, M., & Liu, Q. (2012). Experimental study of distributor diffuser plate. *Science Technology and Engineering*, *12*(11), 2631-2636. https://doi.org/10.3969/j.issn.1671-1815.2012.11.026

Liang, H. X., Suo, J. Q., & Li, M. (2013, June 3-7). *Experimental study of the flow and pressure drop performances in advanced combustor distributor diffuser*. Proceedings of ASME Turbo Expo 2013: Turbine Technical Conference and Exposition. https://doi.org/10.1115/GT2013-94209.

Meng, X., Zuo, Z., Nishi, M., & Liu, S. (2020). A numerical study on the flow mechanism of performance improvement of a wide-angle diffuser by inserting a short splitter vane. *Processes*, *8*(2), 143. https://doi.org/10.3390/pr8020143.

Sanal Kumar, V. R., Abhijit, M., Khan, Y., Arokkiaswamy, A., & Gemson, R. M. O. (2007, July 8-11). *Studies on dump diffusers for modern aircraft engines*. 43rd AIAA/ ASME/ SAE/ ASEE Joint Propulsion Conference & Exhibit. https://doi.org/10.2514/6.2007-5161.

Shen, J. J., Gao, A. S., Gao, T. T., & Zhao, J. Z. (2021). Optimization of extraction technology of sterols from discarded soybean pod by response surface methodology. *Environmental Challenges*, *5*, 100272. https://doi.org/10.1016/j.envc.2021.100272.

Shen, S., He, P., Shang, M., & Mao, R. (2014, June 16-20). *The effects of cowling geometry, area ratio and dump gap on a combustor diffusion system*. Proceedings of ASME Turbo Expo 2014: Turbine Technical Conference and Exposition, Volume 4B. https://doi.org/10.1115/gt2014-26652.

Smith, J. M., & Juhasz, A. J. (1978). Performance of a short Annular Dump Diffuser using suction-stabilized vortices at Inlet Mach Numbers to 0.41 NASA Technical Paper 1194.

Srinivasan, R., Freeman, G., Grahmann, J., & Coleman, E. (1990, July 16-18). *Parametric evaluation of the aerodynamic performance of an annular combustor-diffuser system*. 26th Joint Propulsion Conference. https://doi.org/10.2514/6.1990-2163.

Sun, S. S., Zhu, Y. M., Gu, Z. S., Chu, H. Y., Hu, C. S., Gao, L. J., & Zhao, X. F. (2020). Mechanical properties of ZSM-5 extruded catalysts: calcination process optimization using response surface methodology. *Journal of Chemical Engineering Communications*, *13*(9), 6108-6123. https://doi.org/10.1080/00986445.2020.1803295.

Taguchi, G. (1990). Introduction to quality engineering，Tokyo. *Asian Productivity Organization*, *4*(2), 10-15. http://worldcat.org/isbn/9283310845.

Walker, A. D., & Denman, P. A. (2005). Hybrid diffusers for radially staged combustion systems. *Journal of Propulsion and Power*, *21*(2), 264-273. https://doi.org/10.2514/1.6680.

Walker, A. D., Carrotte, J. F., & McGuirk, J. J. (2009). The influence of dump gap on external combustor aerodynamics at high fuel injector flow rates. *Journal of Engineering for Gas Turbines and Power*, *131*(3), 031506. https://doi.org/10.1115/1.3028230.

Walker, A. D., Denman, P. A., & McGuirk, J. J. (2004). Experimental and computational study of hybrid diffusers for gas turbine combustors. *Journal of Engineering for Gas Turbines and Power*, *126*(4), 717-725. https://doi.org/10.1115/1.1772403.

Wu, Y. L., Zhu, Y. J., Song, S., Wu, Y. N., & Hu, S. Q. (2022). Optimize the preservation effect of mint, clove and chitosan on fresh-cut apple by response surface methodology. *Science and Technology of Food Industry*, *43*(3), 317-324. https://doi.org/10.13386/j.issn1002-0306.2021050258.

Xiang, H. H., Hou, M. J., & Liu, Z. G. (2014). Correlative analysis of performance experimental data of axial flow fans/ compressors based on statistical characteristic. *Journal of Aerospace Power*, *29*(01), 146-152. https://doi.org/10.13224/j.cnki.jasp.2014.01.019.

Yan, C., Yu, J., Xu, J. L., Fan, J. J., Gao, R. Z., & Jiang, Z. H. (2011). On the achievement and prospects for the methods of computational fluid dynamics. *Advances in Mechanics*, *41*(5), 562-589. https://doi.org/10.1631/jzus.A1000257

Zhang, P., Zhang, C., & Wang, Z. (2022). Optimization of crescent-shaped block downstream a row of cylindrical holes to enhance film cooling effectiveness. *Journal of Thermal Analysis and Calorimetry*, *2022*(147), 11205-11219. https://doi.org/10.1007/s10973-022-11346-z.

Zhao, C. C., Suo, J. Q., Liang, H. X., & Wang, J. Z. (2014). Further research for single-plate annular distributor type diffuser performance. *Journal of Propulsion and Technology*, *35*(9), 1241-1246. https://doi.org/10.13675/j.cnki.tjjs.2014.09.013